Available online at www.sciencedirect.com

SciVerse ScienceDirect

journal homepage: www.elsevier.com/locate/he

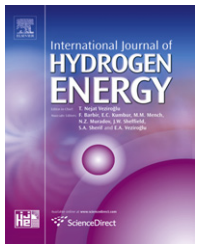

2D thermal modeling of a solid oxide electrolyzer cell (SOEC) for syngas production by H_2O/CO_2 co-electrolysis

*Meng Ni**

Building Energy Research Group, Department of Building and Real Estate, The Hong Kong Polytechnic University, Hung Hom, Kowloon, Hong Kong, China

ARTICLE INFO

Article history:
Received 22 December 2011
Received in revised form
14 January 2012
Accepted 18 January 2012
Available online 11 February 2012

Keywords:
Solid oxide fuel cell
Heat transfer
Synthetic fuel
Co-electrolysis
Thermo-electrochemical model

ABSTRACT

Solid oxide fuel cells (SOFCs) can be operated in a reversed mode as electrolyzer cells for electrolysis of H_2O and CO_2. In this paper, a 2D thermal model is developed to study the heat/mass transfer and chemical/electrochemical reactions in a solid oxide electrolyzer cell (SOEC) for H_2O/CO_2 co-electrolysis. The model is based on 3 sub-models: a computational fluid dynamics (CFD) model describing the fluid flow and heat/mass transfer; an electrochemical model relating the current density and operating potential; and a chemical model describing the reversible water gas shift reaction (WGSR) and reversible methanation reaction. It is found that reversible methanation and reforming reactions are not favored in H_2O/CO_2 co-electrolysis. For comparison, the reversible WGSR can significantly influence the co-electrolysis behavior. The effects of inlet temperature and inlet gas composition on H_2O/CO_2 co-electrolysis are simulated and discussed.

1. Introduction

Solid oxide fuel cells (SOFCs) are promising electrochemical devices for clean power generation. At typical working temperatures (i.e. 1073 K), SOFCs can be operated with renewable biofuels as internal reforming of hydrocarbon fuels can occur in the porous anode [1–4]. In addition, the waste heat from SOFC stacks can be recovered by integrating with other thermodynamic cycles for combined power and heating/cooling cogeneration. Apart from generating electricity, SOFCs can be operated in a reversed mode as solid oxide electrolyzer cells (SOECs) for H_2 production by H_2O electrolysis [5–10]. Compared with H_2 production by low temperature electrolyzers, such as proton exchange membrane electrolyzers and alkaline electrolyzers, steam electrolysis by SOEC can be achieved at a lower operating potential and consumes less electrical energy [10]. Due to their potential for large-scale H_2 production, SOECs have received increasing attention and several projects have been initiated by the US Department of Energy (DOE) [11,12]. There are also growing interests in integrating SOECs with nuclear energy and geothermal energy technologies to optimize the H_2 production efficiency [13,14]. Several mathematical models have been developed to simulate the physical–chemical processes in SOECs at different levels [15–20]. It is found that the transport characteristics in SOECs differ significantly from SOFCs [21], thus the results from SOFCs may not be applicable to SOECs. In addition to steam electrolysis for H_2 production, CO_2 electrolysis using SOECs has been studied for O_2 production by US NASA [22–24]. Several groups also demonstrated the feasibility of H_2O/CO_2 co-electrolysis for simultaneous production of H_2 and CO [25–29]. Co-electrolysis of H_2O and CO_2 in SOECs is much more complicated than electrolysis of H_2O or CO_2, respectively. This is because the reversible water gas shift

* Tel.: +852 2766 4152; fax: +852 2764 5131.
E-mail addresses: bsmengni@inet.polyu.edu.hk, memni@graduate.hku.hk.

0360-3199/$ – see front matter
doi:10.1016/j.ijhydene.2012.01.072

reaction (WGSR, Eq. (1)) and methanation reaction/reversed direct internal steam reforming (DIR) reaction (Eq. (2)) may occur in the porous cathode. In the literature, WGSR and DIR are called internal reforming as well.

$$CO + H_2O \rightleftarrows CO_2 + H_2 \quad (1)$$

$$CO + 3H_2 \rightleftarrows CH_4 + H_2O \quad (2)$$

Due to the complex physical/chemical processes involved in the SOEC for co-electrolysis, the coupled transport and reaction phenomenon have not been well understood yet. For example, it is commonly believed that CO may be produced from reversed WGSR (Eq. (1)) or from CO_2 electrolysis, but it is not clear how much CO is produced by reversed WGSR [30–32]. However, in the long run, it doesn't matter which way CO is formed. In addition, CH_4 is usually not observed in the co-electrolysis process [29] but the mechanisms have not been fully understood. In order to clarify the above issues, a 2D thermal model is developed to analyze the coupled heat/mass transfer and chemical/electrochemical reactions in an SOEC for H_2O/CO_2 co-electrolysis. It is based on and extended from the previous models for H_2O electrolysis [6,18] and CO_2 electrolysis [33] as well as a recent electrochemical model for co-electrolysis [34]. The modeling results show that CH_4 formation via reversed steam reforming (Eq. (2)) is not favorable in the co-electrolysis process. However, the reversible WGSR could contribute to the CO production, depending on the operating conditions.

2. The model

The computational domain and working mechanism of a planar SOEC for H_2O/CO_2 co-electrolysis are shown in Fig. 1. Typical thicknesses of cell components are summarized in Table 1. In operation, a mixture consisting of H_2O, CO_2, H_2, CO, and CH_4 is supplied to the inlet of SOEC cathode and air is supplied to the anode channel. It is considered that the reversible methanation reaction (reversed internal reforming, Eq. (1)) and reversible water gas shift reaction (WGSR, Eq. (2)) can occur in the porous cathode layer, depending on the operating conditions.

Table 1 – Parameters used in simulation.

Parameter	Value
Operating temperature, T (K)	1073
Operating pressure, P (bar)	1.0
Electrode porosity, ε	0.4
Electrode tortuosity, ξ	3.0
Average pore radius, r_p (μm)	0.5
Cathode-supported	
Cathode thickness d_c (μm)	500
Electrolyte thickness, L (μm)	100
Anode thickness, d_a (μm)	100
Height of gas flow channel (mm)	1.0
Length of the planar SOEC (mm)	20
Thickness of interconnect (mm)	0.5
Inlet velocity: U_{in} (m s^{-1})	1.0
Anode inlet gas molar ratio: O_2/N_2	0.21/0.79
Molar Fractions of H_2O and CO_2 at the cathode inlet[a]	0.5/0.5
SOEC operating potential (V)	1.5V
Thermal conductivity of SOEC component (W m^{-1} K^{-1})	
Cathode	11.0
Electrolyte	2.7
Anode	6.0
Interconnect	1.1

a Various molar fractions are studied in the parametric simulations.

The H_2O and CO_2 molecules can diffuse through the porous cathode to the triple phase boundary (TPB) at the cathode-electrolyte interface, where they react with electrons to produce H_2 and CO, as well as O^{2-} (Eqs. (3) and (4)). The produced oxygen ions are transported through dense electrolyte to the TPB at the anode-electrolyte interface, where they lose electrons to form O_2 (Eq. (5)).

$$H_2O + 2e^- \rightarrow H_2 + O^{2-} \quad (3)$$

$$CO_2 + 2e^- \rightarrow CO + O^{2-} \quad (4)$$

$$2O^{2-} \rightarrow O_2 + 4e^- \quad (5)$$

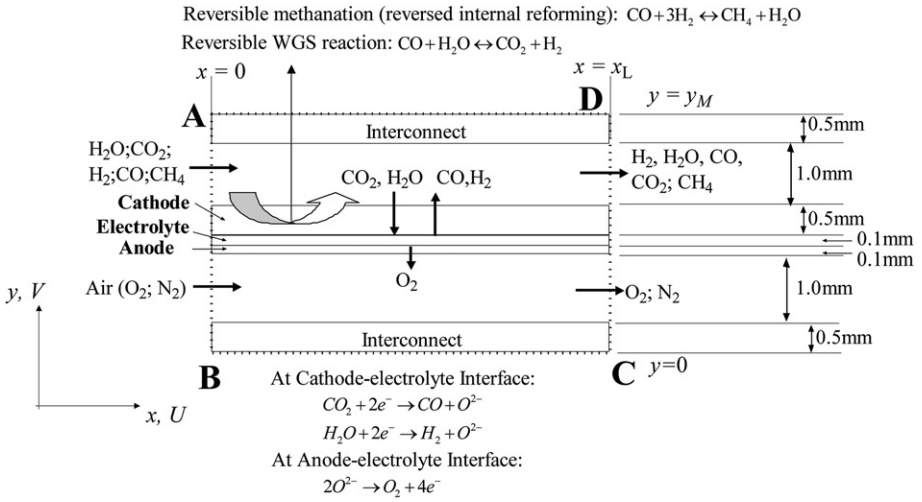

Fig. 1 – Computational domain of the SOEC for co-electrolysis of H_2O and CO_2.

Based on the working mechanisms, a 2D thermal model is developed to study the coupled heat/mass transfer and chemical/electrochemical reactions in the planar SOEC used for co-electrolysis of H_2O and CO_2. The model consists of 3 sub-models: a computational fluid dynamics (CFD) model simulating the fluid flow and heat/mass transfer; an electrochemical model calculating the current density distribution at given operating potentials; and a chemical model calculating the reversible WGSR and reversible methanation reaction rates.

2.1. CFD model

In an SOEC, fluid flow and mass transfer occur in the cathode/anode channels and the porous electrodes. Meanwhile, heat transfer occurs in the whole computational domain. In the porous electrodes, local thermal equilibrium condition is assumed. The governing equations for mass conservation, momentum conservation, energy conservation are summarized below [18].

$$\frac{\partial(\rho U)}{\partial x}+\frac{\partial(\rho V)}{\partial y}=S_m \tag{6}$$

$$\frac{\partial(\rho UU)}{\partial x}+\frac{\partial(\rho VU)}{\partial y}=-\frac{\partial P}{\partial x}+\frac{\partial}{\partial x}\left(\mu\frac{\partial U}{\partial x}\right)+\frac{\partial}{\partial y}\left(\mu\frac{\partial U}{\partial y}\right)+S_x \tag{7}$$

$$\frac{\partial(\rho UV)}{\partial x}+\frac{\partial(\rho VV)}{\partial y}=-\frac{\partial P}{\partial y}+\frac{\partial}{\partial x}\left(\mu\frac{\partial V}{\partial x}\right)+\frac{\partial}{\partial y}\left(\mu\frac{\partial V}{\partial y}\right)+S_y \tag{8}$$

$$\frac{\partial(\rho c_P UT)}{\partial x}+\frac{\partial(\rho c_P VT)}{\partial y}=\frac{\partial}{\partial x}\left(k\frac{\partial T}{\partial x}\right)+\frac{\partial}{\partial y}\left(k\frac{\partial T}{\partial y}\right)+S_T \tag{9}$$

$$\frac{\partial(\rho UY_i)}{\partial x}+\frac{\partial(\rho VY_i)}{\partial y}=\frac{\partial}{\partial x}\left(\rho D_{i,m}^{eff}\frac{\partial Y_i}{\partial x}\right)+\frac{\partial}{\partial y}\left(\rho D_{i,m}^{eff}\frac{\partial Y_i}{\partial y}\right)+S_{sp} \tag{10}$$

where U and V are the velocity components in x and y directions; ρ is the density of gas mixture, μ is the viscosity of the gas mixture; k is the thermal conductivity; c_p is the heat capacity; $D_{i,m}^{eff}$ is the effective diffusion coefficient of species i in gas mixture, which can be found in the previous publications [35]. Both ρ and μ depend on the local gas composition and temperature and the gas mixture is treated as ideal gas in the present study. In the porous electrodes, effective heat conductivity and heat capacity are used and can be calculated as [36],

$$k=\varepsilon k_f+(1-\varepsilon)k_s \tag{11}$$

$$c_p=\varepsilon c_{p,f}+(1-\varepsilon)c_{p,s} \tag{12}$$

where ε is the electrode porosity; k_f and k_s are the heat conductivity (W m^{-1} K^{-1}) of the fluid and solid, respectively; $c_{p,f}$ and $c_{p,s}$ are the heat capacity (J kg^{-1} K^{-1}) of the fluid and solid, respectively. Similar to ρ and μ, both k and c_p are temperature-dependent.

The source term in Eq. (6) represents the mass consumption in the cathode and mass generation in the anode due to electrochemical reactions (Eqs. (3)–(5)). In Eq. (10), the source term represents the gas consumption/generation due to chemical/electrochemical reactions (Eqs. (1)–(5)). The Darcy's law ($S_x=-\frac{\mu U}{Bg}$ and $S_y=-\frac{\mu V}{Bg}$) is used as source terms in momentum equations (Eqs. (7) and (8)) so that the momentum equations are applicable for both the gas channels and the porous electrodes, by assigning a suitable permeability (B_g) to the porous electrodes and an infinitely large permeability to the gas channels. The source term in energy equation (Eq. (9)) represents heat generation or absorption by chemical/electrochemical reactions as well as heat generation by irreversible overpotential losses [37,38]. Detailed descriptions of the source terms and their calculation methods can be found in the previous publications [37,38].

The source terms in species equation (Eq. (10)) and energy equation (Eq. (9)) are related to chemical/electrochemical reactions. Thus an electrochemical model and a chemical model are needed to calculate the rate of electrochemical/chemical reactions.

2.2. Electrochemical model

The electrochemical reaction rate at a given voltage is linked with the current density, which can be calculated by the electrochemical model. In operation, the required voltage applied to the SOEC can be calculated as,

$$V=E+\eta_{act,a}+\eta_{act,c}+\eta_{ohmic} \tag{13}$$

where E is the equilibrium potential, which can be calculated by Eqs. (14) and (15) for H_2O electrolysis and CO_2 electrolysis respectively [38].

$$E_{H_2}=1.253-0.00024516T+\frac{RT}{2F}\ln\left[\frac{P_{H_2}^{I}\left(P_{O_2}^{I}\right)^{0.5}}{P_{H_2O}^{I}}\right] \tag{14}$$

$$E_{CO}=1.46713-0.0004527T+\frac{RT}{2F}\ln\left[\frac{P_{CO}^{I}\left(P_{O_2}^{I}\right)^{0.5}}{P_{CO_2}^{I}}\right] \tag{15}$$

In Eqs. (14) and (15), $P_{H_2}^{I}$, $P_{H_2O}^{I}$, $P_{CO_2}^{I}$, P_{CO}^{I} and $P_{O_2}^{I}$ are the partial pressures of H_2, H_2O, CO_2, CO and O_2 at the electrolyte–electrode interface, respectively. Therefore, the concentration overpotentials are implicitly included in the Nernst potentials. R is the universal gas constant (8.3145 J mol^{-1}K^{-1}). F is the Faraday constant (96,485 C mol^{-1}). η_{ohmic} is the ohmic overpotential and can be calculated by the Ohm's law [6]. $\eta_{act,a}$ and $\eta_{act,c}$ are the activation overpotentials at the anode and cathode, respectively. $\eta_{act,a}$ and $\eta_{act,c}$ are assumed to vary linearly with current density as [38],

$$\eta_{act,H_2,i}=\frac{RTJ_{H_2}}{n_{H_2}FJ_{H_2,i}^{0}} \tag{16}$$

$$\eta_{act,CO,i}=\frac{RTJ_{CO}}{n_{CO}FJ_{CO,i}^{0}} \tag{17}$$

where $J_{H_2,i}^{0}$ and $J_{CO,i}^{0}$ are the exchange current densities for electrolysis of H_2O and CO_2, respectively. The subscript i ($i=a$ and c) means the anode and cathode, respectively. n_{CO} and n_{H_2} are the number of electrons (2 in the present study) transferred per reaction (CO_2 electrolysis and H_2O electrolysis). The details on the exchange current densities can be found in a previous publication [38].

2.3. Chemical model

In this study, it is considered that reversible WGSR and reversible methanation reaction (reversed direct internal reforming reaction: DIR) can take place but the actual direction and magnitude of the reaction rates depends on the operating conditions. In the literature, the Haberman and Young's model is widely used for calculating the reversible WGSR rate (R_{WGSR}, mol m^{-3} s^{-1}) and reversible DIR reaction rates (R_{DIR}, mol.m^{-3}.s^{-1}) [39], thus it is adopted in the present study.

$$R_{WGSR} = k_{sf}\left(p_{H_2O}p_{CO} - \frac{p_{H_2}p_{CO_2}}{K_{ps}}\right) \quad (18)$$

$$k_{sf} = 0.0171\exp\left(\frac{-103191}{RT}\right)\ \text{mol.m}^{-3}.\text{Pa}^{-2}.\text{s}^{-1} \quad (19)$$

$$K_{ps} = \exp(-0.2935Z^3 + 0.6351Z^2 + 4.1788Z + 0.3169) \quad (20)$$

$$Z = \frac{1000}{T(K)} - 1 \quad (21)$$

$$R_{DIR} = k_{rf}\left(P_{CH_4}P_{H_2O} - \frac{P_{CO}(P_{H_2})^3}{K_{pr}}\right) \quad (22)$$

$$k_{rf} = 2395\exp\left(\frac{-231266}{RT}\right) \quad (23)$$

$$K_{pr} = 1.0267 \times 10^{10} \times \exp(-0.2513Z^4 + 0.3665Z^3 + 0.5810Z^2 - 27.134Z + 3.277) \quad (24)$$

The heat generation/consumption due to chemical reactions can be calculated according to corresponding enthalpy changes [40]. Between 600 K and 1200 K, the reaction heat (J mol^{-1}) for reversible WGSR and reversible DIR reaction can be approximated as [38,40],

$$H_{DIR} = -(206205.5 + 19.5175T) \quad (25)$$

$$H_{WGSR} = 45063 - 10.28T \quad (26)$$

2.4. Numerical scheme

The finite volume method (FVM) is used to solve the governing equations in the CFD model [41,42]. The boundary conditions can be found in Ref. [43], i.e. adiabatic conditions are applied at the bottom and the top of the computation zone ($y = 0$ and $y = y_M$). SIMPLEC algorithm is used to couple the velocity and pressure. A TDMA-based alternative iteration scheme is employed to solve the discretized equations. The electrochemical model and chemical model are solved in each iteration to update the source terms for the CFD sub-model. In the electrochemical model, the current densities for H_2O electrolysis and CO_2 electrolysis are determined using their respective Nernst potentials and overpotential losses [44–46]. Computation is repeated until convergence is achieved. The in-house code is written in FORTRAN. The CFD model has been validated in the previous publications [18,43]. In previous studies, the mean temperature of the SOEC is found to match the inlet temperature at thermal neutral voltages for electrolysis of H_2O and CO_2, thus the model is reliable for simulating the thermal field of the SOEC [18,33]. The chemical model and electrochemical model have been validated in refs. [34,47].

3. Results and discussion

The dimensions and typical structural/operating parameters for H_2O/CO_2 co-electrolysis are summarized in Table 1. At the cathode inlet, a small value (1%) of CH_4 molar fraction is used to examine the variation of methanation/internal reforming reaction in SOECs.

3.1. Effect of operating temperature

Fig. 2a and b show the effect of operating temperature on the distributions of current density in an SOEC, at an operating potential of 1.5 V, inlet gas velocity of 0.5 m s^{-1}, and inlet gas composition (molar fraction) of H_2O: 49.9%; CO_2: 50%; CH_4: 0.1%. The total current density in Fig. 2b is the sum of current

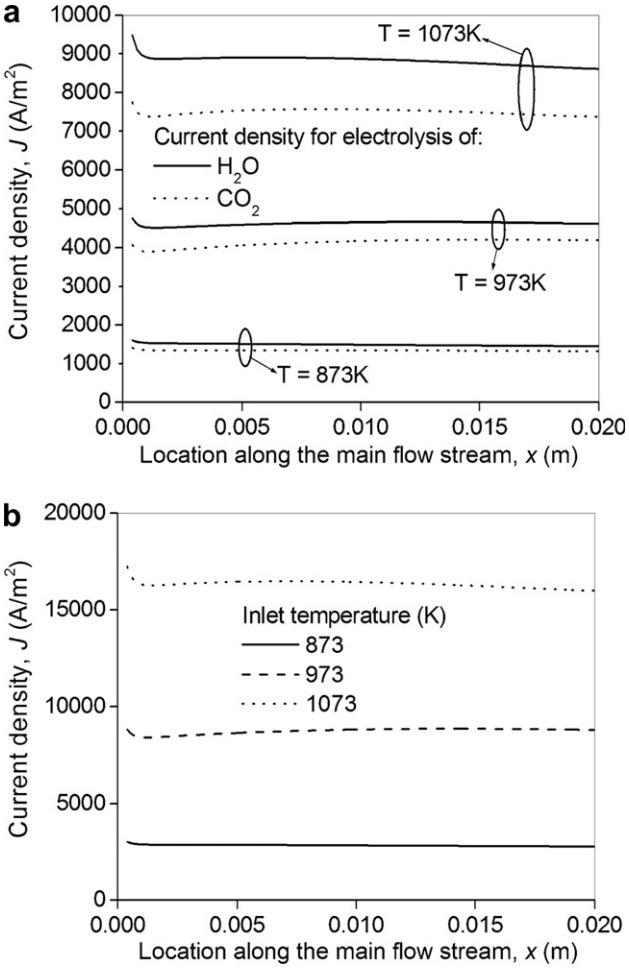

Fig. 2 – Effect of inlet temperature on current density distribution in SOEC, with inlet H_2O molar fraction of 49.9%, CO_2 molar fraction of 50%, CH_4 molar fraction of 0.1%, inlet gas velocity of 0.5 m s^{-1}; and operating potential of 1.5 V; (a) current density for electrolysis of H_2O and CO_2; (b) total current density.

densities for H_2O electrolysis and CO_2 electrolysis. The current densities for electrolysis of H_2O and CO_2 are found to increase considerably with an increase in temperature. This is because both activation overpotential and ohmic overpotential decrease considerably with increasing temperature. In addition, at a higher temperature, the difference in current densities for electrolysis of H_2O and CO_2 are enlarged (Fig. 2a). This is because the equilibrium potential under standard conditions for CO_2 electrolysis is lower than that for H_2O electrolysis, i.e. at 1200 K, 0.923869 V for CO_2 electrolysis and 0.940172 V for H_2O electrolysis [34].

To gain a fundamental understanding of the coupled transport and reaction phenomena in SOEC, the distributions of gas species' molar fraction, rates of reversible WGSR and reversible reforming reaction, temperature, and velocity ratio are shown in Figs. 3 and 4. Due to electrolysis of H_2O and CO_2, the molar fractions of H_2 and CO are found to increase along the SOEC main flow stream (Fig. 3a and b). The difference in H_2 molar fraction between the porous cathode and the cathode channel is small, indicating fast H_2 diffusion in the porous electrode and low concentration overpotential for H_2O electrolysis (Fig. 3a). For comparison, the CO molar fraction in the porous cathode is considerably higher than that in the cathode channel, indicating slow diffusion of CO and a larger loss due to mass transfer for CO_2 electrolysis (Fig. 3b). For example, near the outlet, the CO molar fraction at the

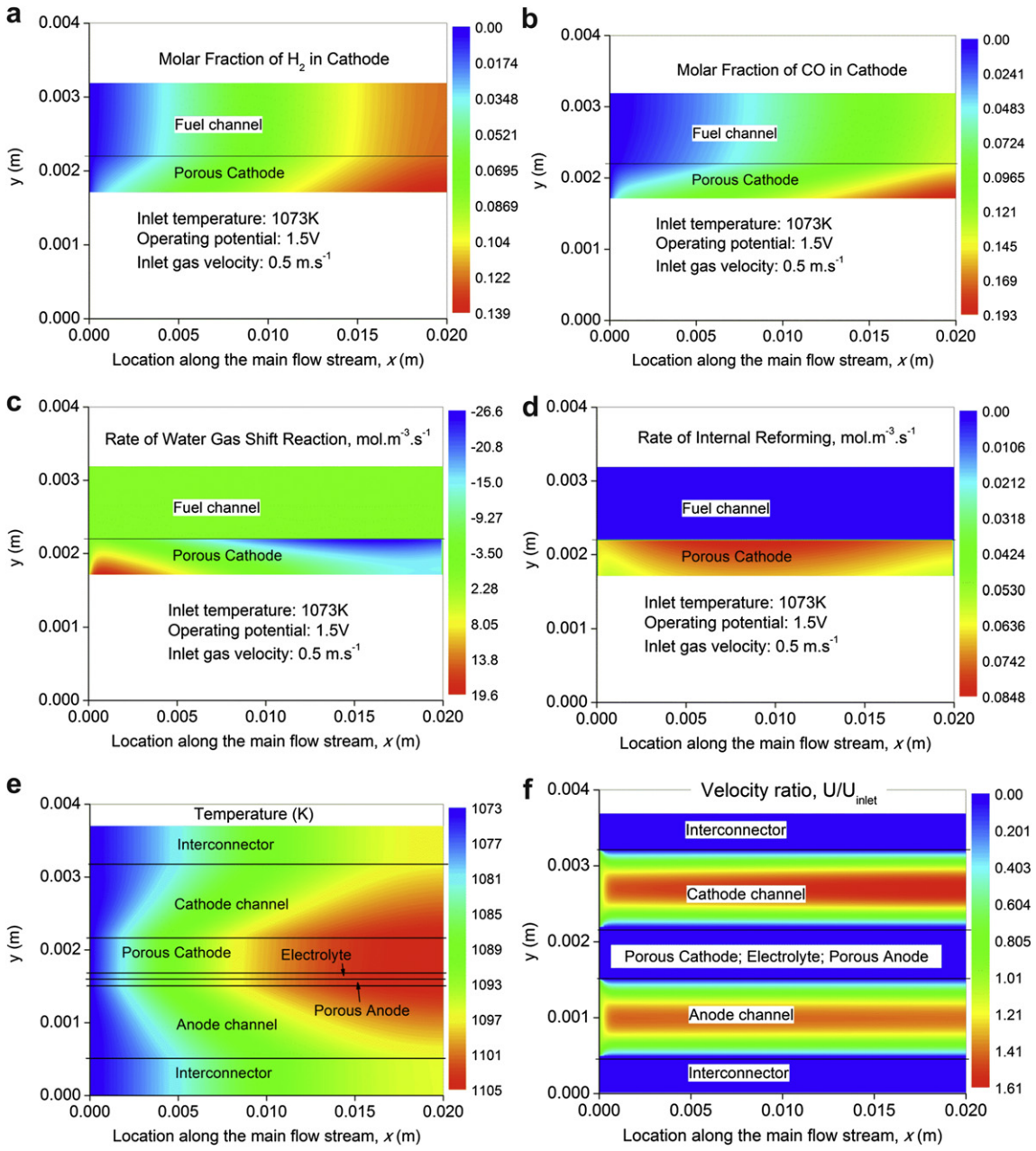

Fig. 3 – Performance of SOEC at an inlet temperature of 1073 K and operating potential of 1.5 V – (a) H_2 molar fraction in cathode; (b) CO molar fraction in cathode; (c) rate of reversible WGSR; (d) rate of reversible DIR; (e) temperature; (f) velocity ratio.

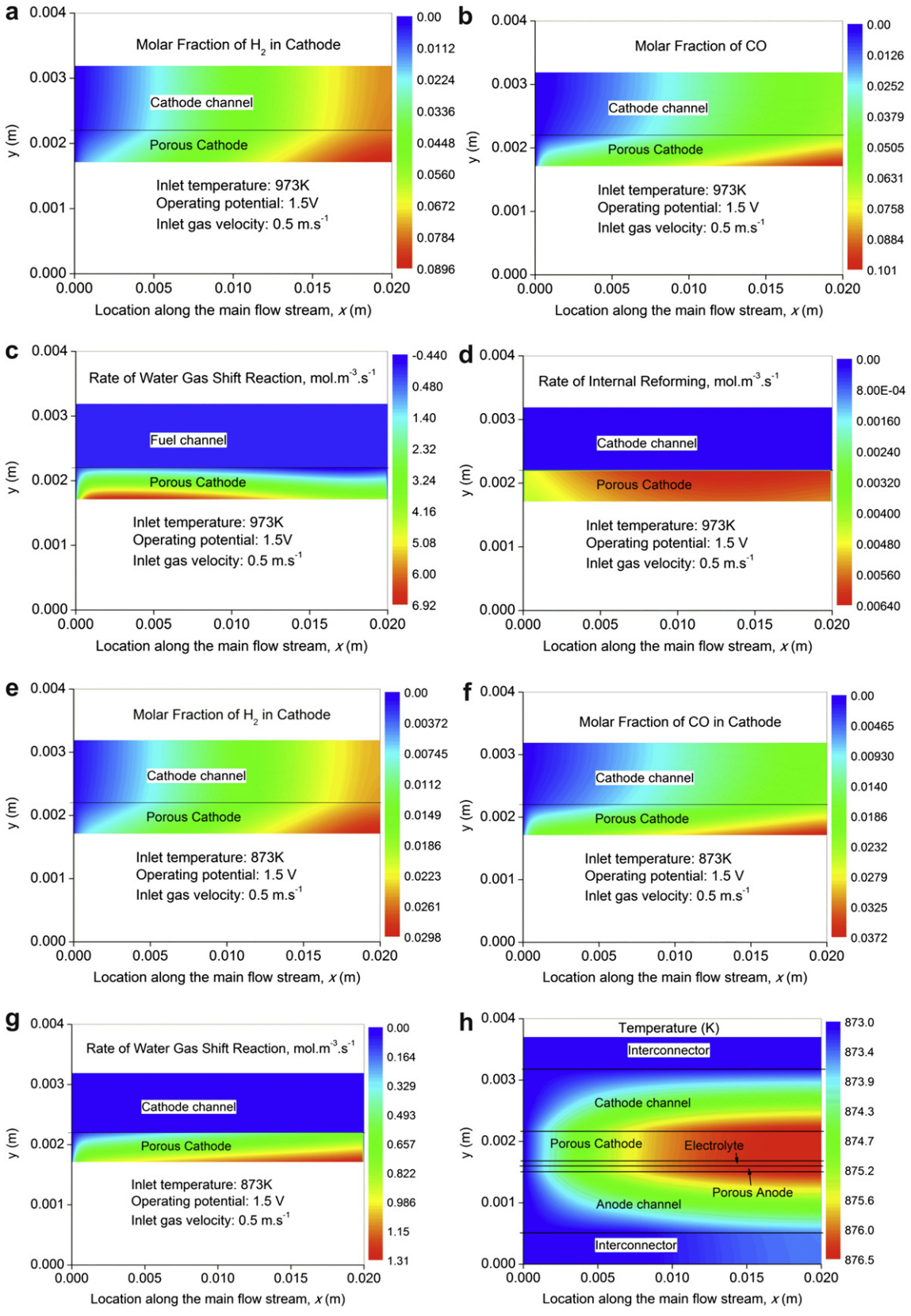

Fig. 4 – Performance of SOEC at inlet temperature of 973 K (4a–d) or 873 K (4e–h) and operating potential of 1.5 V – (a) H_2 molar fraction at 973 K; (b) CO molar fraction at 973 K; (c) rate of WGSR at 973K; (d) rate of DIR at 973 K; (e) H_2 molar fraction at 873 K; (f) CO molar fraction at 873 K; (g) rate of WGSR at 873 K; (h) temperature distribution at an inlet temperature of 873 K.

cathode-electrolyte interface is about 19%, while it is about 13% in the cathode channel (Fig. 3b). This is consistent the results from the literature that the concentration overpotential for CO is usually higher than H_2 fuel [48].

Fig. 3c shows the distribution of reversible WGSR in the cathode of SOEC. The reaction rate of WGSR is positive near the inlet and negative in most of the porous cathode in the downstream. The positive rate of WGSR is caused by relatively high concentration of CO at the cathode-electrolyte interface near the inlet, since CO is more difficult to diffuse to the cathode channel than H_2 due to higher diffusion coefficient of H_2 than CO [18,33,48]. In the downstream, the reversed WGSR is favored due to considerably increased H_2 concentration by H_2O electrolysis. The WGSR rate also varies considerably in the cathode depth. For example, near the outlet, the WGSR reaction rate is decreased from about -26 mol m^{-3} s^{-1} near the cathode surface to about -10 mol m^{-3} s^{-1} at the cathode-electrolyte interface. Since the average reaction rate of WGSR is negative under the present simulation conditions, the reversible WGSR contributes to CO production. This also explains why the molar fractions of H_2 and CO are almost the same at the outlet of the cathode channel (Fig. 3 a and b), despite of higher current density for H_2 production from H_2O electrolysis (Fig. 2). Compared with the reversible WGSR, the reaction rate of reversible DIR is very small and positive (Fig. 3d), means that the methanation (reversed DIR) is not favored for CH_4 production. This is consistent with experimental measurements, from which no CH_4 is detected [29].

Although both H_2O electrolysis and CO_2 electrolysis are endothermic, the cell temperature is increased by about 32 K from 1073 K at the inlet to be about 1105 K at the outlet (Fig. 3e). The temperature field of the SOEC is determined by 3 factors: (1) endothermic electrolysis of H_2O and CO_2; (2) irreversible overpotential losses, which generate heat; and (3) reversible WGSR, which can generate heat for positive reaction rate and consume heat for negative reaction rate (reversed reaction). The effect of WGSR is small due to a small average WGSR rate of the cell. As the operating potential (1.5 V) is higher than the thermal neutral voltages (TNV) for electrolysis of H_2O and CO_2 [18,33], the heat generation from overpotential losses exceeds heat demand for electrolysis reaction. Fig. 3f shows the ratio of local velocity to the inlet velocity in the SOEC. The gas velocity in the porous electrodes is found to be very low (close to 0), while the gas velocity ratio in the gas channels is found to follow the inlet flow pattern near the inlet and fully developed flow pattern in the downstream – increases from the solid surface to the maximum at the center line of the gas channels. The results are consistent with flow field and velocity variation pattern in an SOFC duct [49].

With a decrease in inlet temperature from 1073 K to 973 K and 873 K, the molar fractions of both H_2 and CO are decreased (Fig. 4a,b,e,f), due to considerably reduced current densities for electrolysis of H_2O and CO_2 (Fig. 2). The reaction rate of reversible WGSR is found to decrease significantly with decreasing temperature (Fig. 4c and g). As less CO_2 is consumed by electrolysis and less H_2 is produced from H_2O electrolysis, reversed WGSR is not favored at reduced temperature, as can be seen from positive reaction rate of WGSR in Fig. 4c and g. For comparison, the reversible DIR reaction rate is still negligibly small at various operating temperatures (Fig. 4d), indicating that both CH_4 formation and reforming are not favored in co-electrolysis of H_2O and CO_2. At a reduced current density, the heat generation by overpotential losses is also reduced. Thus, the temperature increase along the main flow stream is found to decrease from about 32 K (between outlet and inlet) at 1073 K to be about 3.5 K at an inlet temperature of 873 K (Fig. 4h).

3.2. *Effect of inlet gas composition*

Fig. 5 shows the effect of inlet gas molar fraction on performance of SOEC for H_2O/CO_2 co-electrolysis. Two cases are considered in the present study. In case 1, the inlet gas molar fractions for H_2O and CO_2 are 75% and 25%, respectively. In case 2, the inlet gas molar fractions for H_2O and CO_2 are 25% and 75%, respectively.

It is found that the current densities for H_2O electrolysis and CO_2 electrolysis in case 1 are higher than in case 2 (Fig. 5a). This finding is out of expectation, since CO_2 electrolysis should not be favored with a lower concentration of CO_2, but the corresponding current density is higher in case 1 than in case 2, especially in the downstream. This phenomenon is caused by the different reaction rates of WGSR in the SOEC (Fig. 5b and c). In case 1, much larger molar fraction of H_2O than that of CO_2 favors forward reaction of WGSR thus the WGSR rate is positive in case 1 (Fig. 5b). For comparison, backward reaction of WGSR is favored with large molar fraction of CO_2, leading to strongly negative reaction rate of WGSR in case 2 (Fig. 5c).

Due to higher current density for H_2O electrolysis and positive reaction rate of WGSR, the H_2 molar fraction increases considerably along the SOEC cell and reaches about 17% at the outlet in case 1 (Fig. 5d), significantly higher than that in case 2 (about 7–8% at the outlet, Fig. 5e). Although the current density for CO_2 electrolysis in case 1 is slightly higher than in case 2, the strongly positive reaction rate of WGSR consumes CO. The combined effects result in lower molar fraction of CO in case 1 than in case 2 (Fig. 5f and g).

3.3. *Effect of operating potential*

The effect of operating potential on co-electrolysis behaviors of an SOEC is shown in Fig. 6. As expected, the current density increases with increasing operating potential (Fig. 6a), leading to higher rate of electrolysis for H_2O and CO_2.

Near the inlet of the SOEC, the reversible WGSR is primarily positive and the reaction rate is increased with an increase in operating potential from 1.0 V to 1.5 V (Fig. 6b and c). This is consistent with the previous 1D study that reversible WGSR could be positive and consume CO at a high potential under certain operating conditions [34]. However, in the downstream, the reversible WGSR become reversed due to significant change in gas composition (Fig. 6b and c). At a lower operating potential (i.e. 1.0 V), the reversible WGSR rate is negative near the cathode surface and positive near the cathode-electrolyte interface, in the downstream of the SOEC (Fig. 6b). This is because of a higher concentration of CO_2 and H_2 at the cathode surface due to fast diffusion of H_2. For comparison, near the cathode-electrolyte interface, relatively higher CO molar fraction (due to slow diffusion rate to the

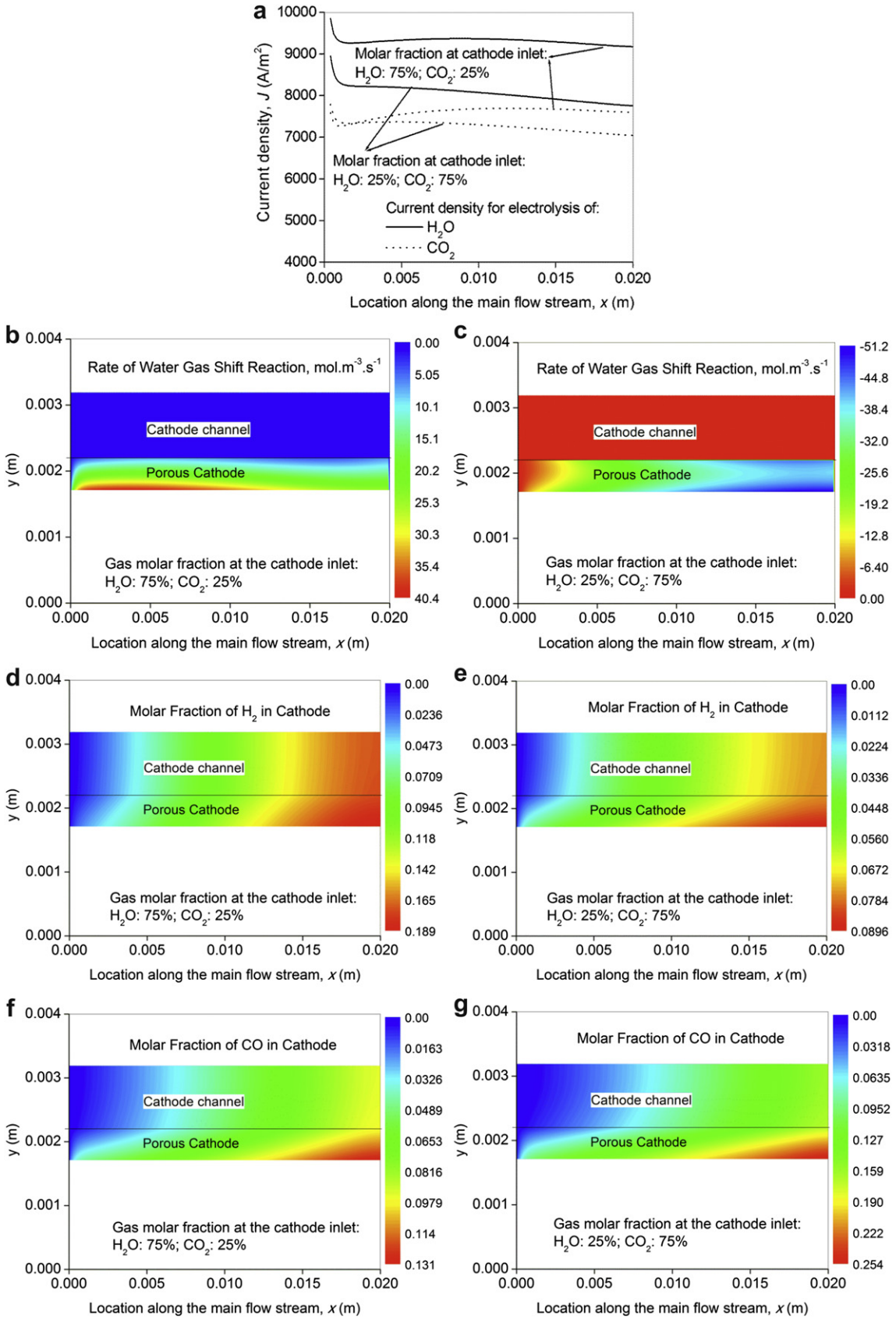

Fig. 5 – Effect of inlet gas composition on SOEC performance. Case 1 – H_2O: 75%; CO_2: 25%; Case 2 – H_2O: 25%; CO_2: 75%. (a) distribution of current density; (b) rate of WGSR for case 1; (c) rate of WGSR for case 2; (d) H_2 molar fraction for case 1; (e) H_2 molar fraction for case 2; (f) CO molar fraction for case 1; (g) CO molar fraction for case 2.

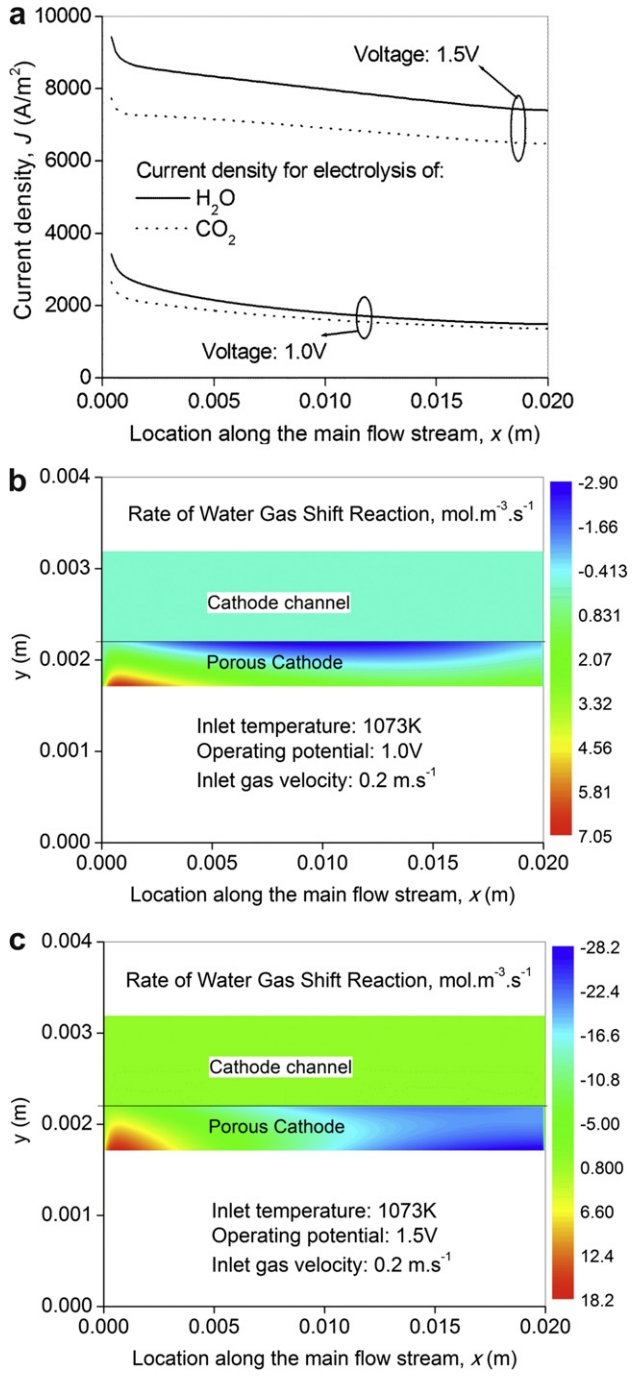

Fig. 6 – Effect of operating potential on SOEC performance at inlet gas velocity of 0.2 m s^{-1} with inlet gas molar fractions of H_2O: 50% and CO_2: 50%; inlet temperature: 1073 K – (a) current density distribution; (b) rate of WGSR at 1.0 V; (c) rate of WGSR at 1.5 V.

cathode surface) favors positive reaction rate of WGSR (Fig. 6b). At a higher operating potential (i.e. 1.5 V), the reversible WGSR is negative (Fig. 6c), due to high rate of H_2 production by H_2O electrolysis, as can be seen from Fig. 6a.

From the above analyses, it can be seen that 1D electrochemical model can serve as the basis for 2D thermal-electrochemical analyses. However, it should be also mentioned that due to large variations of gas composition along the flow channel, the chemical/electrochemical reaction rates vary significantly. Therefore, the conclusions drawn from 1D model may not be directly applicable to 2D cell and need to include the variation along the flow stream. In addition, the porous microstructure also influences the co-electrolysis processes, as it determines the diffusion resistance for gas flow in the porous media. For example, smaller pore size can cause large diffusion resistance and high concentration polarization loss. Analyses of the microstructural effects can be found in the previous studies conducted by the author or other researchers [43,49].

4. Conclusions

In this paper, a 2D thermal model is developed to predict the performance of an SOEC used for H_2O/CO_2 co-electrolysis for H_2/CO syngas production. Both the reversible WGSR and DIR reaction are included in the model.

Simulations are performed at inlet temperatures of 873 K, 973 K and 1073 K. It is found that methanation reaction (reversed DIR reaction) is not favored, which is consistent with experimental observations in the literature. For comparison, the effect of reversible WGSR on the co-electrolysis behavior is significant and cannot be neglected. The WGSR could contribute to CO production or consume CO, depending on various operating conditions. Under the simulation conditions with an inlet gas composition (molar fraction) of H_2O: 50% and CO_2: 50%, the magnitude of WGSR reaction rate is found to increase with increasing temperature and reversed WGSR is favored at a high temperature. At an inlet temperature of 1073 K, current densities for electrolysis of both H_2O and CO_2 are found to increase when the inlet gas composition is changed from case 2 (H_2O: 25%; CO_2: 75%)to case 1 (H_2O: 75%; CO_2: 25%). With an increase in operating potential from 1.0 V to 1.5 V, current densities for co-electrolysis are increased considerably. However, the reversible WGSR contributes to CO production at 1.5 V as the rate of WGSR is strongly negative in the downstream. The 2D modeling results presented in this paper provide good information on the underlying processes pertinent to the SOEC operation, and may guide the future design optimization.

Acknowledgment

This research was supported by a grant (No. A-PK48) from The Hong Kong Polytechnic University, Hong Kong.

REFERENCES

[1] Singhal SC, Kendall K. High temperature solid oxide fuel cells – Fundamentals, design and applications. New York: Elsevier; 2003.
[2] Colpan CO, Dincer I, Hamdullahpur F. Thermodynamic modeling of direct internal reforming solid oxide fuel cells operating with syngas. Int J Hydrogen Energy 2007;32:787–95.

[3] Shiratori Y, Ijichi T, Oshima T, Sasaki K. Internal reforming SOFC running on biogas. Int J Hydrogen Energy 2010;35:7905–12.
[4] Achenbach E, Riensche E. Methane/steam reforming kinetics for solid oxide fuel cells. J Power Sources 1994;52:283–8.
[5] Ni M, Leung MKH, Leung DYC. Technological development of hydrogen production by solid oxide electrolyzer cell (SOEC). Int J Hydrogen Energy 2008;33:2337–54.
[6] Ni M, Leung MKH, Leung DYC. Parametric study of solid oxide steam electrolyzer for hydrogen production. Int J Hydrogen Energy 2007;32:2305–13.
[7] Ni M, Leung MKH, Leung DYC. Electrochemical modeling of hydrogen production by proton-conducting solid oxide steam electrolyzer. Int J Hydrogen Energy 2008;33:4040–7.
[8] Hawkes G, O'Brien J, Stoots C, Hawkes B. 3D CFD model of a multi-cell high temperature electrolysis stack. Int J Hydrogen Energy 2009;34:4189–97.
[9] Stephen Herring J, O'Briend JE, Stoots CM, Hawkes GL, Hartvigsen JJ, Shahnam M. Progress in high-temperature electrolysis for hydrogen production using planar SOFC technology. Int J Hydrogen Energy 2007;32:440–50.
[10] Ni M, Leung MKH, Leung DYC. Energy and exergy analysis of hydrogen production by solid oxide steam electrolyzer plant. Int J Hydrogen Energy 2007;32:4648–60.
[11] Rund JA. System design and new materials for reversible solid-oxide, high-temperature steam electrolysis. US DOE Hydrogen Program, FY; 2005. Progress Report. pp. 361–362.
[12] Hartvigsen J, Swank D, Schade C, Bordia R. Large area cell for hybrid hydrogen co-generation process. US DOE Hydrogen Program, FY; 2005. Progress Report. pp. 367–369.
[13] Yildiz B, Kazimi MS. Efficiency of hydrogen production systems using alternative nuclear energy technologies. Int J Hydrogen Energy 2006;31:77–92.
[14] Sigurvinsson J, Mansilla C, Lovera P, Werkoff F. Can high temperature steam electrolysis function with geothermal heat? Int J Hydrogen Energy 2007;32:1174–82.
[15] Udagawa J, Aguiar P, Brandon NP. Hydrogen production through steam electrolysis: model-based dynamic behavior of a cathode-supported intermediate temperature solid oxide electrolysis cell. J Power Sources 2008;180:46–55.
[16] Udagawa J, Aguiar P, Brandon NP. Hydrogen production through steam electrolysis: control strategies for a cathode-supported intermediate temperature solid oxide electrolysis cell. J Power Sources 2008;180:354–64.
[17] Ni M, Leung MKH, Leung DYC. Mathematical modeling of the coupled transport and electrochemical reactions in solid oxide steam electrolyzer for hydrogen production. Electrochim Acta 2007;52:6707–18.
[18] Ni M. Computational fluid dynamics modeling of a solid oxide electrolyzer cell for hydrogen production. Int J Hydrogen Energy 2009;34:7795–806.
[19] Laurencin J, Kane D, Delette G, Deseure J, Fefebvre-Joud F. Modeling of solid oxide steam electrolyser: impact of the operating conditions on hydrogen production. J Power Sources 2011;196:2080–93.
[20] Rashkeev SN, Glazoff MV. Atomic-scale mechanisms of oxygen electrode delamination in solid oxide electrolyzer cells. Int J Hydrogen Energy 2012;37:1280–91.
[21] Ni M, Leung MKH, Leung DYC. A modeling study on concentration overpotentials of a reversible solid oxide fuel cell. J Power Sources 2006;163:460–6.
[22] Tao G, Sridhar KR, Chan CL. Study of carbon dioxide electrolysis at electrode/electrolyte interface: part 1. Pt/YSZ interface. Solid State Ionics 2004;175:615–9.
[23] Tao G, Sridhar KR, Chan CL. Study of carbon dioxide electrolysis at electrode/electrolyte interface: part II. Pt-YSZ cermet/YSZ interface. Solid State Ionics 2004;175:621–4.
[24] Sridhar KR, Vaniman BT. Oxygen production on Mars using solid oxide electrolysis. Solid State Ionics 1997;97:147–52.
[25] O'Brien JE, McKellar MG, Harvego EA, Stoots CM. High temperature electrolysis for large scale hydrogen and syngas production from nuclear energy – summary of system simulation and economic analyses. Int J Hydrogen Energy 2010;35:4808–19.
[26] Ebbesen SD, Hogh J, Nielsen KA, Nielsen JU, Mogensen M. Durable SOC stacks for production of hydrogen and synthesis gas by high temperature electrolysis. Int J Hydrogen Energy 2011;36:7363–73.
[27] Kim-Lohsoontorn P, Bae J. Electrochemical performance of solid oxide electrolysis cell electrodes under high-temperature coelectrolysis of steam and carbon dioxide. J Power Sources 2011;196:7161–8.
[28] Stoots C, O'Brien J, Hartvigsen J. Results of recent high temperature coelectrolysis studies at the Idaho National Laboratory. Int J Hydrogen Energy 2009;34:4208–15.
[29] Zhan ZL, Kobsiriphat W, Wilson JR, Pillai M, Kim I, Barnett SA. Syngas production by co-electrolysis of CO_2/H_2O: the basis for a renewable energy cycle. Energy Fuels 2009;23:3089–96.
[30] Graves C, Ebbesen SD, Mogensen M. Co-electrolysis of CO_2 and H_2O in solid oxide cells: performance and durability. Solid State Ionics 2011;192:398–403.
[31] Stoots CM, O'Brien JE, Herring JS, Hartvigsen JJ. Syngas production via high-temperature coelectrolysis of steam and carbon dioxide. J Fuel Cell Sci Technol 2009;6:011014.
[32] Ebbesen SD, Graves C, Mogensen M. Production of synthetic fuels by co-electrolysis of steam and carbon dioxide. Int J Green Energy 2009;6:646–60.
[33] Ni M. Modeling of a solid oxide electrolysis cell for carbon dioxide electrolysis. Chem Eng J 2010;164:246–54.
[34] Ni M. An electrochemical model for syngas production by co-electrolysis of H_2O and CO_2. J Power Sources 2012;202:209–16.
[35] Ni M. Thermo-electrochemical modeling of ammonia-fueled solid oxide fuel cells considering ammonia thermal decomposition in the anode. Int J Hydrogen Energy 2011;36:3153–66.
[36] Yuan JL, Lv XR, Sunden B, Yue D. Analysis of parameter effects on transport phenomena in conjunction with chemical reactions in ducts relevant for methane reformers. Int J Hydrogen Energy 2007;32:3887–98.
[37] Ni M. On the source terms of species equations in fuel cell modeling. Int J Hydrogen Energy 2009;34:9543–4.
[38] Ni M. Modeling of SOFC running on partially pre-reformed gas mixture. Int J Hydrogen Energy 2012;37:1731–45.
[39] Haberman BA, Young JB. Three-dimensional simulation of chemically reacting gas flows in the porous support structure of an integrated-planar solid oxide fuel cell. Int J Heat Mass Transfer 2004;47:3617–29.
[40] Chase MW. NIST-JANAF thermochemical tables. 4th ed. American Chemical Society, American Institute of Physics for the National Institute of Standards and Technology; 1998.
[41] Patankar SV. Numerical heat transfer and fluid flow. New York (: McGraw-Hill; 1980.
[42] Wang CY. Fundamental models for fuel cell engineering. Chem Rev 2004;104:4727–65.
[43] Ni M. 2D thermal-fluid modeling and parametric analysis of a planar solid oxide fuel cell. Energ Convers Manage 2010;51:714–21.
[44] Iwai H, Yamamoto Y, Saito M, Yoshida H. Numerical simulation of intermediate-temperature direct-internal-reforming planar solid oxide fuel cell. Energy 2011;36:2225–34.

[45] Wang QS, Li LJ, Wang C. Numerical study of thermoelectric characteristics of a planar solid oxide fuel cell with internal reforming of methane. J Power Sources 2009;186:399–407.
[46] Zinovik I, Poulikakos D. Modeling the temperature field in the reforming anode of a button-shaped solid oxide fuel cell. Electrochim Acta 2009;54:6234–43.
[47] Ni M, Leung DYC, Leung MKH. Modeling of methane fed solid oxide fuel cells: comparison between proton conducting electrolyte and oxygen ion conducting electrolyte. J Power Sources 2008;183:133–42.
[48] Suwanwarangkul R, Croiset E, Fowler MW, Douglas PL, Entchev E, Douglas MA. Performance comparison of Fick's, dusty gas and Stefan-maxwell models to predict the concentration overpotential of a SOFC anode. J Power Sources 2003;122:9–18.
[49] Yuan JL, Rokni M, Sunden B. Three-dimensional computational analysis of gas and heat transport phenomena in ducts relevant for anode-supported solid oxide fuel cells. Int J Heat Mass Transfer 2003;46: 809–21.